

Metallomics

Accepted Manuscript



This is an *Accepted Manuscript*, which has been through the Royal Society of Chemistry peer review process and has been accepted for publication.

Accepted Manuscripts are published online shortly after acceptance, before technical editing, formatting and proof reading. Using this free service, authors can make their results available to the community, in citable form, before we publish the edited article. We will replace this *Accepted Manuscript* with the edited and formatted *Advance Article* as soon as it is available.

You can find more information about *Accepted Manuscripts* in the [Information for Authors](#).

Please note that technical editing may introduce minor changes to the text and/or graphics, which may alter content. The journal's standard [Terms & Conditions](#) and the [Ethical guidelines](#) still apply. In no event shall the Royal Society of Chemistry be held responsible for any errors or omissions in this *Accepted Manuscript* or any consequences arising from the use of any information it contains.

Cite this: DOI: 10.1039/c0xx00000x

www.rsc.org/xxxxxx

ARTICLE TYPE

Identification of dopaminergic neurons of the substantia nigra pars compacta as a target of manganese accumulation[‡]

Gregory Robison^a, Brendan Sullivan^a, Jason R. Cannon^b, Yulia Pushkar^{*a}

Received (in XXX, XXX) Xth XXXXXXXXXX 20XX, Accepted Xth XXXXXXXXXX 20XX

DOI: 10.1039/b000000x

Manganese serves as a cofactor to a variety of proteins, necessary for proper bodily development and function. However, an overabundance of Mn in the brain can result in manganism, a neurological condition resembling Parkinson's disease (PD). Bulk sample measurement techniques have identified the globus pallidus and thalamus as targets of Mn accumulation in the brain, however smaller structures/cells cannot be measured. Here x-ray fluorescence microscopy determined the metal content and distribution in the substantia nigra (SN) of the rodent brain. *In vivo* retrograde labeling of dopaminergic cells (via FluoroGoldTM) of the SN pars compacta (SNc) subsequently allowed for XRF imaging of dopaminergic cells *in situ* at subcellular resolution. Chronic Mn exposure resulted in a significant Mn increase in both the SN pars reticulata (>163%) and the SNc (>170%) as compared to control; no other metal concentrations were significantly changed. Subcellular imaging of dopaminergic cells demonstrated that Mn is located adjacent to the nucleus. Measured intracellular manganese concentrations range between 40–200 μM ; concentrations as low as 100 μM have been observed to cause cell death in cell cultures. Direct observation of Mn accumulation in the SNc could establish a biological basis for movement disorders associated with manganism, specifically Mn caused insult to the SNc. Accumulation of Mn in dopaminergic cells of the SNc may help clarify the relationship between Mn and the loss of motor skills associated with manganism.

Introduction

Neurodegenerative diseases often present a spectrum of symptoms ranging from mood variations to motor impairments. Parkinson's disease (PD) is the most prevalent disorder in which loss of dopaminergic (DA) neurons within the substantia nigra pars compacta (SNc) results in motor dysfunction. The exact cause of PD is unknown, however environmental pollutants may play a role; one such pollutant is manganese (Mn). Manganese is required for normal body development and functions and its dietary intake is regulated by limited absorption in gut. Exposure to Mn via inhalation or injection, routes which bypass the gut, can increase Mn accumulation in the brain resulting in Mn-induced motor dysfunction (i.e. *manganism*). Cases of manganism are reported in miners^{1,2}, welders, smelters^{3,4}, and abusers of ephedrine/methcathinone^{5,6}. Additionally, patients suffering from liver dysfunction demonstrate Mn poisoning due to decreased removal of Mn from the blood^{7,8}. The commonality of symptoms shared between PD and advanced manganism suggests a potential relationship between the diseases; see review articles^{9–11}. For this reason, various epidemiological studies have examined the correlation between increased occupational and/or environmental Mn exposure and incidence of PD^{12–19}. While it has been found that key proteins in the PD etiology exhibit

differential expression under Mn exposure^{20–22}, a recent critical review on epidemiology of PD concludes that the evidence for Mn as environmental factor remains inadequate²³.

Studies using cell cultures consistently demonstrate that DA neurons are susceptible to Mn exposure^{20, 24–29}. However, these experiments fail to model the effects of the blood-brain and blood-cerebrospinal fluid barriers on Mn access to the brain and distribution of Mn amongst different brain structures. Magnetic resonance imaging of Mn distribution in brain is a powerful technique for medical diagnosis of Mn exposure *in vivo* which has reported increased T₁ weighted signal intensity in the SN of primates and humans^{9, 30–32}. Current resolutions fall short of single cell imaging. Conversely, techniques which can provide subcellular resolution require ultra-thin samples and cannot be used for large-area imaging (e.g. electron energy loss spectroscopy) or have limited sampling volumes and therefore have not been used for Mn quantification (e.g. secondary ion mass spectroscopy). X-ray fluorescence (XRF) microscopy presents an alternative approach, permitting the use of thick ($\geq 10 \mu\text{m}$), unfixed samples for Mn quantification with a range of possible resolutions (0.03–100 μm)^{24, 25, 33–35}.

Here we report quantitative XRF imaging of Mn in SNc and SNr of rat model of Mn induced neurotoxicity. Identification of DA neurons of the SNc while maintaining physiological metal concentrations presents an additional difficulty for *in situ*

measurements. Immunohistochemical (IHC) staining for tyrosine hydroxylase (TH) would identify DA cells, however Mn leaching from the tissue has been observed following staining of tissue³⁴. Here, we addressed the difficulty of *in situ* cell identification by administering FluoroGold™ (FG) retrograde tracer during survival surgery to label DA cells of the SNc *in vivo*. Only a sub-population of cells of the SNc accumulate FG, however of these cells, a high percentage (>98%) are immunopositive for TH^{36,37}. We show that DA neurons are preferential targets of Mn accumulation in the rodent brain. The spatial distribution of Mn in these cells is permissive to reactivity with dopamine which could be a cause of toxicity.

Experimental Procedures

Animals

Adult male Sprague Dawley® outbred rats were purchased from Harlan (Indianapolis, IN) at the age of 8 weeks (225-249 g). Rats were maintained on Purina rodent chow 5001 containing 70 ug g⁻¹ Mn content. Upon receipt, rats were housed in a 12 h/12 h light/dark room and allowed access to rat chow and distilled, de-ionized water *ad libitum*. A 3-day acclimation period followed receipt of the animals before initiating treatment protocol.

Treatment

Animals were randomly divided into 2 experimental groups for treatment; One group underwent chronic Mn exposure via intraperitoneal (i.p.) injections of MnCl₂ in sterile saline (6 mg of Mn per kilogram body weight, 109 mM) while the control group received saline injections of the same volume. Injections were performed weekdays for a period of 4 weeks. At the conclusion of the treatment protocol a 24-hour waiting period was observed prior to animal sacrifice. Animals that underwent FluoroGold™ (Fluorochrome, LLC) retrograde tracer injections underwent a Mn/saline treatment protocol with survival surgery being performed at the end of 4 weeks followed by an additional 2 weeks of Mn/saline treatment prior to sacrifice. FluoroGold™ was dissolved in 0.9% saline solution to a final concentration of 2% w/v. Prior to administration rats were anesthetized by inhalation of 2-5% isoflurane which was then maintained at 1-3% during the surgery. The scalp was shaved and disinfected with betadine for 1 minute after which an incision was made to reveal the bregma point on the skull. A burr hole was drilled at bregma 2.25 mm and a microsyringe was inserted to the depth of the caudate putamen. The FG solution (0.2 µL) was injected over the course of five minutes. The microsyringe was then removed, the burr hole sealed, and the scalp closed with stitches. Ketoprofen (5 mg kg⁻¹ subcutaneous) was administered as an analgesic before surgery and every 24 h afterwards for up to 72 h. All experiments complied with animal rights regulations and were approved by the Institutional Committee on Animal Use at Purdue University.

Sacrifice and tissue sectioning

Prior to sacrifice, animals were anesthetized with a solution containing ketamine (75 mg kg⁻¹) and xylazine (10 mg kg⁻¹) via i.p. injection. Unconsciousness occurs within several minutes of

Table 1: XRF imaging parameters

Beamline	Pixel size (µm × µm)	Dwell (s)	Flux (photons s ⁻¹)	Figure
8 BM-B	25 × 25	2-4	3.5 × 10 ¹⁰	Fig. 1, S2A Fig. S1A Fig. S1B Fig. S1C Fig. 3B
18 ID-D	20 × 20	0.5-1	1.8 × 10 ¹¹	
2 ID-D	10 × 10	0.5	4 × 10 ⁹	
2 ID-E	2 × 2	0.5	5 × 10 ⁸	Fig. 3C, S3A-B
	0.3 × 0.3	0.5-2		
	1 × 1	0.5-4		
	0.5 × 0.5			

injection; an additional injection was administered as necessary in the event that the initial injection was insufficient. Unconsciousness was assessed by performing a tail pinch or eye tap. Sacrifice was performed by severing the iliac artery and draining the blood from the animal; the brain stem was then severed resulting in death. After removing the skin, the skull was peeled away to reveal the brain, which was removed using spatula onto a clean Kim-wipe. The brain was blotted to remove excess blood from the surface and snap frozen in liquid nitrogen. Once completely frozen, as verified by a change in sample color, the sample was wrapped in foil and placed in -80 °C freezer for long term storage. No chemical fixation was used to avoid modifications of metal distribution. Sectioning was performed using a cryotome at an ambient cutting temperature of -12 °C. Coronal sections 10-30 µm thick were collected from bregma -5.20 mm on X-ray compatible supports and on glass slides. Samples were returned to -80 °C until measured.

Data collection

Samples from FG treated animals were imaged using a Leica DM6000 fluorescence microscope at 10× magnification with a DAPI filter cube set (BP360/40, 400, BP470/40) at room temperature to identify FG accumulating cells. A XRF scan of the same area was then performed with 1 µm × 1 µm resolution to obtain K and Zn images to identify individual cells. Comparison of the XRF image with the optical fluorescence image confirmed the location of FG accumulating cells. Samples from non-FG treated animals were XRF imaged at low resolution (10 µm × 10 µm) and the area of high Mn signal was taken as the SNc (Fig. S1A). Higher resolution images (2 µm × 2 µm) were taken and elevated intracellular Zn content within the SNc was assumed to represent the nuclei of DA cells based on preliminary data (Fig. S1B). Single cell images taken at 0.3 µm × 0.3 µm were then taken and used for analysis (Fig. S1C). Tissue level scans of the SN were performed at the Advanced Photon Source (APS) Sector 8 BM and Sector 18 ID (BioCAT) beamlines and cell level scans were performed at APS Sector 2ID-D and ID-E beamlines. All scans were carried out at room temperature in a helium environment with the exception of BioCAT measurements which were performed in atmosphere. Parameters used for XRF imaging are presented in Table 1. Fitting of XRF imaging spectra was performed using the MAPS program³⁸ and quantification of areal content performed using either NBS1832/1833 or an AXO thin film XRF reference standard. Standards were measured under the same experimental conditions as the samples. To convert from areal content to concentration, the sample is assumed to be of uniform thickness with an average density of 1 g cm⁻³.

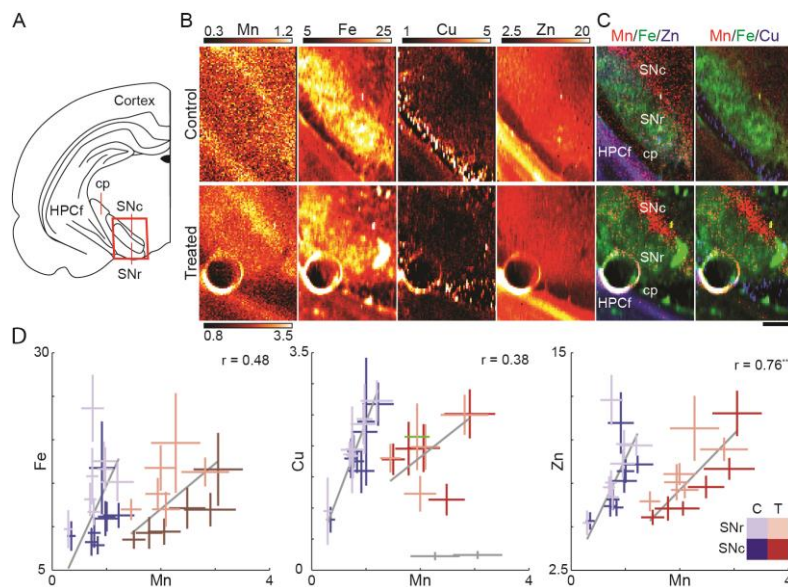


Fig. 1 Tissue level XRF analysis of the SN. (A) Schematic of the coronal plane illustrating the substantia nigra (SN). The substantia nigra pars reticulata (SNr) separates the hippocampal formation (HPCf) and the substantia nigra pars compacta (SNc), which accumulates Mn. The red box corresponds to the regions featured in Fig. 1B. For clarity, the cerebral peduncle (cp) is also labeled. (B) XRF images of the SNr and the SNc, identifiable by the strong Fe and Mn signals respectively. The high Zn content to the lower left is due to the CA3 layer of the HPCf. Maximum scale for Mn in control is one-third that of the Mn treated sample for viewing purposes. (C) Tri-colored plots demonstrate the highest Mn accumulation adjacent to the SNr in both control and treated animals. Brain areas of SNr, SNc, caudal peduncle (cp), and HPCf are indicated on the plot. (D) Scatter plots of average metal concentration versus Mn for the SNc (dark tint) and SNr (light tint) for control (blue, $n=16$ points) and Mn treated animals (red, $n=12$ points). Gray lines indicate the best fit of the data weighted according to standard deviation of the individual data points (bars). Grayed data points identified as outliers and not considered for fitting purposes. Pearson correlation coefficient (r) and significance level (** $p<0.01$) are displayed for metal/Mn of treated samples (Table S1). All numbers given are in $\mu\text{g g}^{-1}$.

To verify that counting statistics were above the minimum analyzable limit, a Kolmogorov-Smirnov test for similarity was employed to test K_{α} peaks obtained through two different fitting methods. Specifically, one K_{α} peak was obtained by first summing the pixel spectra followed by fitting whereas the second K_{α} peak was obtained by first fitting the pixel spectra and summing the fitted results. A null result for the Kolmogorov-Smirnov test indicated that the two K_{α} peaks were statistically identical and therefore each individual spectrum had sufficient counting statistics. Several control samples demonstrated a significant difference between the compared peaks for Mn K_{α} and therefore Mn values represent an upper limit of the actual Mn concentration.

Image analysis

For tissue level scans, the boundary of the SN was delineated by hand based on the Fe and Mn signals (Fig. S2A,B). K-means cluster analysis ($n=2$ clusters) of the Fe and Mn signals at equal weights was then employed to identify the SNc and SNr for Mn treated samples. The resulting clusters were then filled to display a continuous region. In control samples, although the increased Mn content of the SNc is visible, it is too low to reliably identify the SNc using a clustering algorithm. Therefore, the SNr and SNc were delineated by hand based on Mn and Fe content, respectively (Fig. S2A,B). A similar approach using clustering was used to delineate the cell nucleus using the Zn signal ($n=3$ clusters) whereas S, Cl, and K signals were used at equal weights to identify the cell body ($n=2$ clusters; Fig. S3A).

Individual pixel data were used to create scatter plots of Mn

versus each of the other metals examined. Three divisions were considered; the entire cell, the nucleus, and the cell body. For a given division, the average metal content of the region was subtracted from each of the pixel values to remove the cell-to-cell variability. A robust linear regression was then applied to the mean-corrected data to obtain the slope and the standard error. Analysis of covariance was used to evaluate changed slopes between Mn treated and control samples in FG and non-FG treated experimental groups ($\alpha=0.05$).

When noted, pixels demonstrating the highest Mn accumulation were identified by applying an iterative threshold selection algorithm³⁹. The average Mn content was then determined using the pixels above the threshold (Fig. S3B).

Results

XRF imaging of the SN

XRF imaging of a rat model of Mn exposure has revealed the SNc as one of the targets of Mn accumulation in the brain³⁴. Here we expand on the previous study by collecting a larger data set of the SNc and substantia nigra pars reticulata (SNr) with increased spatial resolution (Fig. 1). XRF images allow identification of the SNr based on its Fe content, the cerebral peduncle based on Cu content, and the cornu ammonis 3 (CA3) layer of the hippocampal formation (HPCf) due to strong Zn signal. The SNc, a small area several hundred microns wide, is located medially to the SNr (Fig. 1A,B) based on immunohistochemical staining of adjunct sections for tyrosine hydroxylase. This area displayed an increased Mn accumulation

Cite this: DOI: 10.1039/c0xx00000x

www.rsc.org/xxxxxx

ARTICLE TYPE

Table 2: Metal concentrations measured at the tissue level

Region	Group	Mn	Fe	Cu	Zn
SNc	C	1.70 ^a	21.12 ± 5.68	3.79 ± 1.13	14.90 ± 3.62
	T	4.60 ± 1.25 ^{**}	22.64 ± 5.96	3.74 ± 0.99	14.93 ± 4.46
SNr	C	1.59 ^a	30.83 ± 8.44 ⁺⁺	4.01 ± 1.07	16.77 ± 4.38
	T	4.19 ± 0.89 ^{**}	30.15 ± 6.05 ⁺⁺	3.86 ± 0.94	16.43 ± 3.13

Given values are in $\mu\text{g g}^{-1}$ presented as mean \pm std; n=10/11 control (C)/treated (T).

^a Represents an upper limit of the actual concentration

^{**} p<0.01 as compared to control

⁺⁺ p<0.01 as compared to SNc of same experimental group

Quantitative analysis of metal concentrations at the tissue level showed no statistical difference for the two different Mn exposure durations (4 or 6 weeks) for any considered metal (Fig. S4) and therefore FG/Non-FG (see below for explanation) tissue level data were combined.

A significant change in Mn content was observed in Mn treated groups as compared to saline injected control animals in both the SNr (>163%) and SNc (>170%). However, Fe, Cu, or Zn concentrations in the SN did not change as a result of Mn treatment. Comparison of the SNc and SNr within an experimental group demonstrated less than a 10% difference in average Mn concentration (Table 2). The SNc and SNr had statistically different Fe content. Scatter plots of the average metal concentration of the SNc and SNr for Mn treated samples (Fig. 1C) revealed the strongest correlation between Zn and Mn ($r=0.76$, $p<0.01$; Table S1).

25 Retrograde tracing of DAergic neurons

Survival surgery coupled with unilateral FG tracer injection permitted optical identification of cells in the SNc for subsequent XRF imaging. A schematic diagram demonstrates the approximate location of FG tracer injection (Fig. 2A). Injection of FG into the caudate putamen (CPu) resulted in uptake by axonal terminals (Fig. 2B) leading to DA cell body labeling in the SNc (Fig. 2C-D); minimal labeling of DA cells was observed for the contralateral side. This approach resulted in the labeling of DA cells *in vivo* thereby maintaining physiological metal concentrations in the targeted cells (Fig. 3).

Cells labeled by FG were identified in XRF images by comparison of optical fluorescence image with K and Zn distributions (Fig. 3A-B). The strong Zn signal indicates the location of the nucleus^{40, 41} whereas the S, Cl, and K signals help to identify the extent of the soma (Fig. 3C). Manganese content in both the cell nucleus and cell body of treated cells was significantly increased as compared to control samples (Table 3). Tri-colored images show that Mn does not co-localize with either Fe or Cu hotspots but is heterogeneously distributed in the cell body, primarily localizing along the boundary of the strong Zn signal. To account for this heterogeneous distribution, auto-thresholding of Mn content in the cell body (excluding nucleus)

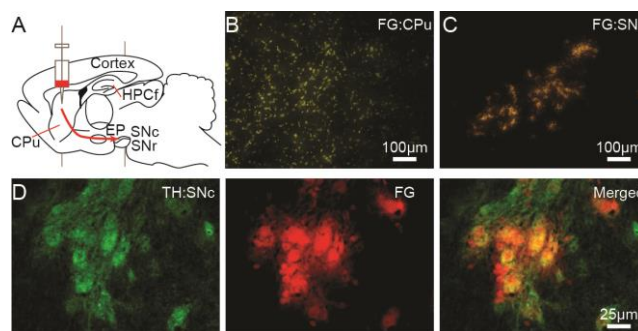


Fig. 2 FG labeling of DA cells. (A) Diagram of a sagittal plane of the rodent brain with the approximate location of FG injection. The red arrow gives an approximate route of the nigra-neostriatum pathway. Injection into the CPu (B) results in uptake into axonal terminals and transport to DA cell bodies of the SNc (C). Scale bars represent a length of 100 μm (10 \times objective). (D) Tyrosine hydroxylase IHC staining (green) reveals a more dense population of DA cells in the SNc than FG tracer (red), however all FG accumulating cells are positive for TH verified by two color image. Scale bars represent a length of 25 μm (40 \times objective).

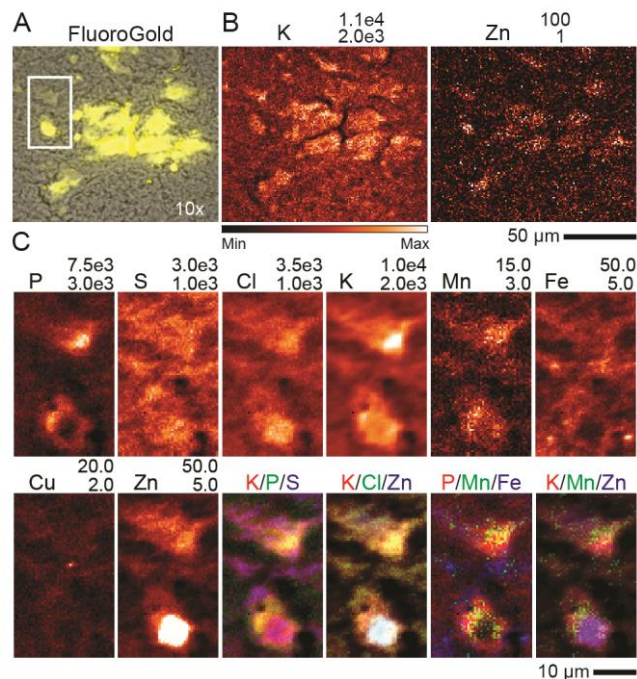


Fig. 3 Optical and XRF imaging of FG, Mn treated rat brain. (A) Brightfield (BF) image of the SNc (gray) with FG fluorescence image overlaid (yellow). Not all dopaminergic cells of the SNc are FG positive. (B) Fly scan XRF image of K and Zn that assist in co-localizing XRF imaging with BF/FG optical images. Dashed white box indicates an area measured at high resolution which contains two cells (C). Example of XRF image recorded at subcellular resolution (0.5 $\mu\text{m} \times 0.5 \mu\text{m}$). A high Zn content was taken to indicate the location of the nucleus. All numbers given are in $\mu\text{g g}^{-1}$.

Table 3 Metal concentration measured from cells

Nucleus Element	Control		Treated	
	Non-FG	FG	Non-FG	FG
P($\times 10^3$)	2.42 \pm 0.12	3.94 \pm 0.65 ⁺	2.84 \pm 0.17	4.01 \pm 0.82 ⁺
K($\times 10^3$)	3.69 \pm 0.19	5.34 \pm 0.38	4.19 \pm 0.11	6.08 \pm 1.56 ⁺
Mn	3.15 \pm 0.28	2.45 \pm 0.17	9.53 \pm 0.93 ^{**}	7.62 \pm 1.06 ^{**}
Fe	11.36 \pm 1.11	26.53 \pm 7.39 ⁺⁺	17.57 \pm 5.72	21.22 \pm 5.84
Cu	2.53 \pm 0.25	4.79 \pm 0.68 ⁺⁺	3.01 \pm 0.50	4.89 \pm 0.81 ⁺⁺
Zn	26.92 \pm 4.49	36.78 \pm 8.59	30.15 \pm 7.63	40.64 \pm 14.07

Cell body Element	Control		Treated	
	Non-FG	FG	Non-FG	FG
P($\times 10^3$)	2.58 \pm 0.16	3.90 \pm 0.57	2.89 \pm 0.32	4.06 \pm 0.95
K($\times 10^3$)	3.57 \pm 0.23	4.82 \pm 0.43	3.85 \pm 0.38	5.50 \pm 1.60
Mn	3.00 \pm 0.22	2.37 \pm 0.19	8.42 \pm 1.50 ^{**}	7.03 \pm 1.23 ^{**}
M _D ^{thresh}	3.62 \pm 0.30	3.21 \pm 0.22	10.95 \pm 1.87 ^{**}	9.08 \pm 1.5 ^{**}
Fe	13.58 \pm 0.48	28.66 \pm 6.90 ⁺⁺	18.10 \pm 2.93	23.52 \pm 6.31
Cu	3.05 \pm 0.13	6.01 \pm 1.30	3.66 \pm 0.56	5.95 \pm 2.13
Zn	18.23 \pm 3.40	21.98 \pm 4.29	18.79 \pm 3.18	22.65 \pm 6.31

Given values are in $\mu\text{g g}^{-1}$ presented as mean \pm std; n=4/5/4/12 control/FlouroGold™ (FG) control/Mn/Mn FG.

⁵ ^{**} p<0.01, ^{*} p<0.05 as compared to control of the same non-FG/FG treatment group

⁺⁺ p<0.01, ⁺ p<0.05 as compared to non-FG sample of the same control/Mn treated group

was applied and resulted in increased average Mn values by 21-35% as compared to the unfiltered average (**Table 3**). The average metal concentration in FG positive cells was consistently higher than that of non-FG treated animals except in Mn content. We attribute this difference to better localization of intact cells in FG samples. Increased phosphorous signals support such possibility and some statistically significant differences in Fe and Cu are removed if concentration of these elements is normalized by phosphorus. Overall cellular metal content imaged *in situ* from brain tissue is highly variable and in some cases the standard deviation within an experimental group was as large as 35% (**Table 3, Fig. S5**).

For additional analysis of Mn distribution in cells, scatter plots of individual pixel concentrations were quantified (**Table S3**). Fe/Mn and Cu/Mn pairs were in general lacking correlation (p<0.30) which reinforces visual lack of co-localization of Mn with Cu or Fe hot spots in the cell. Strong K/Mn and moderate P/Mn correlations were observed for Mn treated groups. A moderate to strong Zn/Mn correlation was observed in the cell body whereas the two metals were uncorrelated in the nucleus. Observed trends are very similar to these reported for single cell imaging in the hippocampal formation on Mn treated rats³⁵ suggesting similar mechanisms of Mn accumulation inside the cell.

Discussion

Animal model

The plasma Mn concentrations in treated animals at day 30 following the dose regimen were between 11-36 $\mu\text{g/L}$ while Mn concentrations in untreated animals were between 3.5-5.6 $\mu\text{g/L}$ ^{42, 43}. For reference, human studies indicate that Mn-poisoned workers usually have blood Mn concentrations in the 4-15 $\mu\text{g/L}$ range and a human study of 39 Mn-poisoned welders in Beijing revealed that the welders with distinct manganism had blood Mn levels between 8.2-36 $\mu\text{g/L}$ ³. A case study involving 3 methcathinone patients reported plasma Mn content was reported as 33-82 $\mu\text{g L}^{-1}$ assuming 55% plasma/blood ratio (v/v; blood Mn content of 18-45 $\mu\text{g L}^{-1}$)⁴⁴. The rodent model of chronic Mn exposure used in this study also demonstrates significantly increased Mn level in brain tissue^{34, 35}.

45

Manganese accumulation in tissue

Accumulation of Mn in the SNr is expected as gabaergic cells of the SNr are functionally and morphologically similar to those of the globus pallidus, which preferentially accumulate Mn upon exposure^{10, 34, 45}. Previous work by this lab has suggested that the SNC as well as SNr accumulates Mn under normal and chronic exposure conditions in the rodent brain³⁴. Manganese concentration in the SNC and the SNr differed by less than 10% (with greater Mn content in the SNC). Tissue concentrations of Mn fall within the predicted range of Mn levels for normal (1.1-2.9 $\mu\text{g g}^{-1}$) and aberrant function (3.2-8.6 $\mu\text{g g}^{-1}$) in humans⁴⁶. Manganese accumulation in Mn treated rodents demonstrated no difference between FG and non-FG treated animals despite a longer treatment time (4 vs. 6 weeks). This result indicates that the total cumulative dose does not accurately reflect the total accumulation of Mn in the brain but rather that a steady state has been achieved with regards to Mn influx/efflux. Although the specific mechanisms are unknown, Mn efflux from the brain has been shown to consist of fast (1-3 d) and slow (1-3 months) clearance mechanisms⁴⁷⁻⁴⁹. It is possible that the Mn load presented to the SN is sufficiently addressed by these mechanism(s).

The combined approach of retrograde tracer labeling and XRF imaging *in situ* quantitatively established Mn accumulation in DA cells. Measurement of DA cell Mn concentration in tissue is particularly novel as cell culture models omit the action of brain barriers. Cellular Mn concentrations from control samples reported here are in agreement with XRF imaging study of pyramidal cells of the CA3 layer of the hippocampal formation³⁵ and the results of Carmona *et al.*²⁴, which observed <3 $\mu\text{g g}^{-1}$ Mn content for untreated cells. These concentrations probably reflects baseline cellular needs in Mn for normal brain cell function.

Average cellular Mn content above the applied threshold for chronic exposure animals is as high as 10.95 $\mu\text{g g}^{-1}$ (200 μM) which high enough to affect cell viability in dopaminergic neuronal cell cultures^{20, 24, 29} although less than the half-maximal inhibitory concentration of 300-1000 μM ^{24, 25, 28}. Note, however, that duration of exposure can have a profound effect. Exposures in cell cultures are usually limited to short periods of time from 3-48 h. Comparison of Mn treated pyramidal and DA cells demonstrate an increased Mn concentration in DA cells (29-59%) highlighting the ability of DA cells to accumulate more Mn. This is in agreement with results reported for PC12 cell culture exposed to 100 μM Mn where similar Mn content of 10 \pm 3 $\mu\text{g g}^{-1}$ was determined using a combined approach of proton induced x-ray emission and backscattering spectrometry²⁴.

Subcellular targets of Mn accumulation

In studies of Mn induced neurotoxicity, attention was foremost given to the subcellular target of Mn accumulation, including the mitochondrion, the nucleus, and recently the Golgi apparatus. The highest Mn concentrations from fractionalized liver cells following acute Mn exposure (i.p. injection of ⁵⁶Mn) were reported in mitochondria (40.6% of total content), followed by the supernatant (28.4%) and the nucleus (16.1%)⁵⁰. However, measurements were taken following suspension of the homogenate in fresh buffer (performed 5 \times) which removed Mn from the organelles to the supernatant. Another study of fractionalized liver cells (4.5 mg kg⁻¹ intravenous injection) observed no statistical difference between

nucleus, cytoplasm, and mitochondria considering Mn content normalized by protein concentration⁵¹. However, that study perfused the liver prior to dissection and re-suspended homogenate only 2×, suggesting that Mn may be more tightly bound to the mitochondrial fraction as compared to the cytoplasm and nucleus. A study using electron energy loss spectroscopy observed dense Mn bodies in mitochondria in brain tissue of rats exposed through drinking water (20 mg mL⁻¹; 100 d) although perfusion removed 50% of the Mn⁵². Similarly, a study using chronic Mn exposure through drinking water (10 mg mL⁻¹; 120 d) noted the highest absolute Mn concentration in fractionalized brain cells was in mitochondria followed by the cytosol and then the nucleus (3-5 washes)⁵³.

In contrast to the above reports, a cell culture study of four immortalized cell lines found that mitochondria contained less than 0.5% of the total Mn content following 24 hour incubation in 100 μM solution and separation involving 4 washes²⁷. Rather, the aforementioned study found that mesencephalic DA neuronal cells (N27) and PC12 cells accumulate more Mn in the soma (35% and 69% of total Mn content respectively) as opposed to brain barrier cell models RBE4 and Z310 which demonstrated substantially lower percentages (5% and 7%). Here we suggest that if Mn were mainly confined to mitochondria, we would observe small (0.5-1 μm in diameter), localized Mn hotspots in the cytoplasm; no such spots were observed. Thus, our results combined with prior studies show that Mn observed in the cell is not preferentially accumulated in mitochondria, is highly mobile, and may be easily modified during cell fractionation, cell fixation and any other manipulations. Our result agree well with other XRF studies of PC12 cell culture which observed Mn in the Golgi apparatus at 100 μM MnCl₂ with an altered distribution at 300 μM²⁴. In that study, accumulation in the Golgi apparatus was confirmed by disrupting the organelle with brefeldin A and observing the subsequent redistribution of Mn in the cell. A recent study further confirmed this assessment via correlative microscopy using Golgi-GFP and XRF imaging of Mn²⁵. XRF imaging studies have reported Mn primarily in the cytoplasm and perinuclear space for GFP-TH positive neurons in mixed neuronal culture exposed to 500 μM MnCl₂ for 3 hours followed by cyrofixation²⁶. Distribution in the soma was also observed in pancreatic β-cells following a 20 minute incubation in 50 μM MnCl₂, 20 minute incubation in 4% paraformaldehyde, several washes, and air drying⁵⁴.

Our study shows sufficiently delocalized (with preferred perinuclear localization) Mn distributions in the DA cells of SNc which have been shown to be susceptible to Mn toxicity upon Mn exposure in culture^{20, 24-29}. Thus, Mn is available to interact with dopamine and with systems of its production, regulation and release. Multiple studies shown that dopamine release in striatum is decreased or impaired under both acute and chronic Mn exposure⁵⁵⁻⁵⁹. One possible explanation is Mn facilitated auto-oxidation of excess DA⁶⁰⁻⁶². Transgenic *Caenorhabditis elegans* expressing DAT loss of function, resulting in increased extracellular DA, are more sensitive to Mn-induced toxicity (9 mM LD50) than wild type controls (47 mM LD50)⁶². Although this has been studied in the context of extracellular DA, DAT is also present on the surface of the endoplasmic reticulum and Golgi apparatus⁶³. Tangentially, DAT inhibition or knockout has been shown decrease Mn content in the rodent globus pallidus and CPU^{45, 64}; it is unclear whether this is directly due to DAT loss of function or to an effect on a Mn

transporter (e.g. DMT-1).

Conclusions

In this study, we found that the SNc is an additional target of Mn accumulation in rats following chronic Mn exposure and demonstrates higher accumulations than previously reported structures, such as the globus pallidus. Furthermore, *in vivo* retrograde tracer administration permitted identification of DA neurons of the SNc using optical fluorescence and XRF imaging allowed for quantification of Mn of these cells *in situ*. The highest Mn content was extranuclear, ranging between 40-200 μM; concentrations above 100 μM have shown to cause cell death in cell culture models^{20, 29}. Together, these findings highlight a possibility of Mn induced malfunction of dopaminergic neurons.

Acknowledgements

We thank Dr. Lan Hong, Dr. Wendy Jiang, and Dr. Wei Zheng of the School of Health Sciences at Purdue University for furnishing the rodent brains used in this study. We also would like to acknowledge Dr. Lydia Finney, Dr. Charlotte Gleber, Dr. Barry Lai, and Evan Maxey for their assistance in operating their respective beamline facilities. We also greatly appreciate the help of Dr. Stefan Vogt in fitting with the MAPS program. Use of the Advanced Photon Source, an Office of Science User Facility operated for the U.S. Department of Energy (DOE) Office of Science by Argonne National Laboratory, was supported by the U.S. DOE under Contract No. DE-AC02-06CH11357. BioCAT is a National Institutes of Health-supported Research Center RR-08630.

Abbreviations

APS	Advanced Photon Source
cp	caudal peduncle
CPu	caudate putamen
CA3	cornus ammonis 3
DA	dopaminergic
FG	FluoroGold™
HPCf	hippocampal formation
i.p.	intraperitoneal
PD	Parkinson's disease
SN	substantia nigra
SNc/r	substantia nigra pars compacta/reticulata
XRF	X-ray fluorescence

Notes and references

^a Department of Physics and Astronomy, Purdue University, 525 Northwestern Ave., West Lafayette, IN, USA. Fax: (765)494-2970; E-mail: grobison@purdue.edu, sullivb@purdue.edu, ypushkar@purdue.edu

^b School of Health Sciences, Purdue University, 550 Stadium Dr., West Lafayette, IN, USA. Fax: (765)494-1377, Tel: (765)494-0794; E-mail: cannonjr@purdue.edu

* To whom correspondence should be addressed: Yulia Pushkar, Department of Physics and Astronomy, Purdue University, 525 Northwestern Ave, West Lafayette, IN 47907, USA. Fax: (765) 494-2970, Tel: (765) 496-3279; E-mail: ypushkar@purdue.edu

† Electronic Supplementary Information (ESI) available: Fig. S1: Identification of non-FG labeled cells in SNc. Fig. S2: Line plots of Mn and Fe in the SN; Fig. S3 Representative example of cell clustering and Mn thresholding results; Fig. S4 Metal content for SNr/c for 4 and 6 week treatment times; Fig S5 Normalized metal content for measured cells. Table S1 Metal/Mn correlations for concentrations measured from tissue. Table

- S2 Cell metal concentrations (combined nucleus and cell body); Table S3 Linear fit parameters for entire cell, nucleus, and cell body.‡ This work was supported by NIH/National Institute of Environmental Health Sciences grants R01 ES008146-14 (W.Z.) and R00 ES019879 (J.R.C.) and by the Purdue University Research Foundation.
1. J. Couper, *British Annals of Medicine, Pharmacy, Vital Statistics, and General Science*, 1837, 1, 41-42.
 2. J. Rodier, *Br. J. Ind. Med.*, 1955, 12, 21-35.
 3. J. Crossgrove and W. Zheng, *NMR Biomed.*, 2004, 17, 544-553.
 4. K. A. Josephs, J. E. Ahlskog, K. J. Klos, N. Kumar, R. D. Fealey, M. R. Trenerry and C. T. Cowl, *Neurology*, 2005, 64, 2033-2039.
 5. A. Stepens, I. Logina, V. Liguts, P. Aldins, I. Eksteina, A. Platkajis, I. Martinsons, E. Terauds, B. Rozentale and M. Donaghy, *N. Engl. J. Med.*, 2008, 358, 1009-1017.
 6. K. Sikk, S. Haldre, S. M. Aquilonius, A. Asser, M. Paris, Ä. Roose, J. Petterson, S. L. Eriksson, J. Bergquist and P. Taba, *European Journal of Neurology*, 2013, 20, 915-920.
 7. P. R. Burkhard, J. Delavelle, R. Du Pasquier and L. Spahr, *Arch. Neurol.*, 2003, 60, 521-528.
 8. L. L. Long, X. R. Li, Z. K. Huang, Y. M. Jiang, S. X. Fu and W. Zheng, *Experimental Biology and Medicine*, 2009, 234, 1075-1085.
 9. T. R. Guilarte, *Environ. Health Perspect.*, 2010, 118, 1071-1080.
 10. C. W. Olanow, *Annals of the New York Academy of Sciences*, 2004, 1012, 209-223.
 11. J. Roth, *NeuroMol. Med.*, 2009, 11, 281-296.
 12. M. M. Finkelstein and M. Jerrett, *Environ. Res.*, 2007, 104, 420-432.
 13. J. M. Gorell, C. C. Johnson, B. A. Rybicki, E. L. Peterson, G. X. Kortsha, G. G. Brown and R. J. Richardson, *Neurology*, 1997, 48, 650-658.
 14. J. M. Gorell, E. L. Peterson, B. A. Rybicki and C. C. Johnson, *J. Neurol. Sci.*, 2004, 217, 169-174.
 15. R. G. Lucchini, E. Albini, L. Benedetti, S. Borghesi, R. Coccaglio, E. C. Malara, G. Parrinello, S. Garattini, S. Resola and L. Alessio, *Am. J. Ind. Med.*, 2007, 50, 788-800.
 16. G. M. Marsh and M. J. Gula, *J. Occup. Environ. Med.*, 2006, 48, 1031-1046.
 17. B. A. Racette, L. McGee-Minnich, S. M. Moerlein, J. W. Mink, T. O. Videen and J. S. Perlmutter, *Neurology*, 2001, 56, 8-13.
 18. B. A. Racette, S. D. Tabbal, D. Jennings, L. Good, J. S. Perlmutter and B. Evanoff, *Neurology*, 2005, 64, 230-235.
 19. A. B. Santamaria, C. A. Cushing, J. M. Antonini, B. L. Finley and F. S. Mowat, *J. Toxicol. Environ. Health, Part B*, 2007, 10, 417-465.
 20. Y. Higashi, M. Asanuma, I. Miyazaki, N. Hattori, Y. Mizuno and N. Ogawa, *J. Neurochem.*, 2004, 89, 1490-1497.
 21. A. D. Gitler, A. Chesi, M. L. Geddie, K. E. Strathearn, S. Hamamichi, K. J. Hill, K. A. Caldwell, G. A. Caldwell, A. A. Cooper, J.-C. Rochet and S. Lindquist, *Nat Genet*, 2009, 41, 308-315.
 22. K. Sriram, G. X. Lin, A. M. Jefferson, J. R. Roberts, O. Wirth, Y. Hayashi, K. M. Krajnak, J. M. Soukup, A. J. Ghio, S. H. Reynolds, V. Castranova, A. E. Munson and J. M. Antonini, *The FASEB Journal*, 2010, 24, 4989-5002.
 23. K. Wirdefeldt, H. O. Adami, P. Cole, D. Trichopoulos and J. Mandel, *Eur. J. Epidemiol.*, 2011, 26, S1-S58.
 24. A. Carmona, G. Deves, S. Roudeau, P. Cloetens, S. Bohic and R. Ortega, *ACS Chem. Neurosci.*, 2010, 1, 194-203.
 25. A. Carmona, S. Roudeau, L. Perrin, G. Veronesi and R. Ortega, *Metalloids*, 2014, 6, 822-832.
 26. T. Dučić, E. Barski, M. Salome, J. C. Koch, M. Bähr and P. Lingor, *J. Neurochem.*, 2013, 124, 250-261.
 27. K. Kalia, W. Jiang and W. Zheng, *Neurotoxicology*, 2008, 29, 466-470.
 28. G. D. Stanwood, D. B. Leitch, V. Savchenko, J. Wu, V. A. Fitsanakis, D. J. Anderson, J. N. Stankowski, M. Aschner and B. McLaughlin, *J. Neurochem.*, 2009, 110, 378-389.
 29. Y. Hirata, *Neurotoxicol. Teratol.*, 2002, 24, 639-653.
 30. O. S. Levin, *Zhurnal Nevrologii I Psikhiiatrii Imeni S S Korsakova*, 2005, 105, 12-20.
 31. M. C. Newland, T. L. Ceckler, J. H. Kordower and B. Weiss, *Exp. Neurol.*, 1989, 106, 251-258.
 32. H. Shinotoh, B. J. Snow, K. A. Hewitt, B. D. Pate, D. Doudet, R. Nugent, D. P. Perl, W. Olanow and D. B. Calne, *Neurology*, 1995, 45, 1199-1204.
 33. A. Daoust, E. L. Barbier and S. Bohic, *NeuroImage*, 2013, 64, 10-18.
 34. G. Robison, T. Zakharova, S. Fu, W. Jiang, R. Fulper, R. Barrea, M. A. Marcus, W. Zheng and Y. Pushkar, *PLoS One*, 2012, 7, e48899.
 35. G. Robison, T. Zakharova, S. Fu, W. Jiang, R. Fulper, R. Barrea, W. Zheng and Y. Pushkar, *Metalloids*, 2013, 5, 1554-1565.
 36. K. B. Seroogy, K. Dangan, S. Lim, J. W. Haycock and J. H. Fallon, *The Journal of Comparative Neurology*, 1989, 279, 397-414.
 37. F. Yao, F. Yu, L. Gong, D. Taube, D. D. Rao and R. G. MacKenzie, *J. Neurosci. Methods*, 2005, 143, 95-106.
 38. S. Vogt, *J. Phys. IV*, 2003, 104, 635-638.
 39. T. W. Ridler and S. Calvard, *IEEE transactions on systems, man, and cybernetics*, 1978, SMC-8, 630-632.
 40. R. S. MacDonald, *Journal of Nutrition*, 2000, 130, 1500S-1508S.
 41. F. Y. H. Wu and C. W. Wu, *Annual Review of Nutrition*, 1987, 7, 251-272.
 42. W. Zheng, Q. Q. Zhao, V. Slavkovich, M. Aschner and J. H. Graziano, *Brain Res.*, 1999, 833, 125-132.
 43. W. Zheng, Y. M. Jiang, Y. S. Zhang, W. D. Jiang, X. Q. Wang and D. M. Cowan, *Neurotoxicology*, 2009, 30, 240-248.
 44. R. A. Hauser, T. A. Zesiewicz, A. S. Rosemurgy, C. Martinez and C. W. Olanow, *Ann. Neurol.*, 1994, 36, 871-875.
 45. J. G. Anderson, P. T. Cooney and K. M. Erikson, *Environ. Toxicol. Pharmacol.*, 2007, 23, 179-184.
 46. A. B. Bowman and M. Aschner, *Neurotoxicology*, 2014, 41, 141-142.
 47. M. C. Newland, C. Cox, R. Hamada, G. Oberdörster and B. Weiss, *Fundam. Appl. Toxicol.*, 1987, 9, 314-328.
 48. A. Takeda, J. Sawashita and S. Okada, *Brain Res.*, 1995, 695, 53-58.
 49. D. Vitarella, B. A. Wong, O. R. Moss and D. C. Dorman, *Toxicol. Appl. Pharmacol.*, 2000, 163, 279-285.
 50. L. S. Maynard and G. C. Cotzias, *Jour Biol Chem*, 1955, 214, 489-495.
 51. P. Ayotte and G. L. Plaa, *Biochem. Pharmacol.*, 1985, 34, 3857-3865.
 52. M. Morello, A. Canini, P. Mattioli, R. P. Sorge, A. Alimonti, B. Bocca, G. Forte, A. Martorana, G. Bernardi and G. Sancesario, *Neurotoxicology*, 2008, 29, 60-72.
 53. J. C. K. Lai, M. J. Minski, A. W. K. Chan, T. K. C. Leung and L. Lim, *Neurotoxicology*, 1999, 20, 433-444.
 54. L. Leoni, A. Dhyani, P. La Riviere, S. Vogt, B. Lai and B. B. Roman, *Contrast Media & Molecular Imaging*, 2011, 6, 474-481.
 55. L. Vidal, M. Alfonso, F. Campos, L. R. F. Faro, R. C. Cervantes and R. Durán, *Neurochem. Res.*, 2005, 30, 1147-1154.
 56. T. R. Guilarte, N. C. Burton, J. L. McGlothlan, T. Verina, Z. Yun, M. Alexander, L. Pham, M. Griswold, D. F. Wong, T. Syversen and J. S. Schneider, *J. Neurochem.*, 2008, 107, 1236-1247.

- 1
2
3
4
5
6
7
8
9
10
11
12
13
14
15
16
17
18
19
20
21
22
23
24
25
26
27
28
29
30
31
32
33
34
35
36
37
38
39
40
41
42
43
44
45
46
47
48
49
50
51
52
53
54
55
56
57
58
59
60
57. T. R. Guilarte, M. K. Chen, J. L. McGlothan, T. Verina, D. F. Wong, Y. Zhou, M. Alexander, C. A. Rohde, T. Syversen, E. Decamp, A. J. Koser, S. Fritz, H. Gonczi, D. W. Anderson and J. S. Schneider, *Exp. Neurol.*, 2006, 202, 381-390.
58. S. A. McDougall, C. M. Reichel, C. M. Farley, M. M. Flesher, T. Der-Ghazarian, A. M. Cortez, J. J. Wacan, C. E. Martinez, F. A. Varela, A. E. Butt and C. A. Crawford, *Neuroscience*, 2008, 154, 848-860.
59. J. Sanchez-Betancourt, V. Anaya-Martínez, A. L. Gutierrez-Valdez, J. L. Ordoñez-Librado, E. Montiel-Flores, J. Espinosa-Villanueva, L. Reynoso-Eraza and M. R. Avila-Costa, *Neurotoxicology*, 2012, 33, 1346-1355.
60. R. Migheli, C. Godani, L. Sciola, M. R. Delogu, P. A. Serra, D. Zangani, G. De Natale, E. Miele and M. S. Desole, *J. Neurochem.*, 1999, 73, 1155-1163.
61. P. A. Serra, G. Esposito, P. Enrico, M. A. Mura, R. Migheli, M. R. Delogu, M. Miele, M. S. Desole, G. Grella and E. Miele, *Br. J. Pharmacol.*, 2000, 130, 937-945.
62. A. Benedetto, C. Au, D. S. Avila, D. Milatovic and M. Aschner, *PLoS Genet.*, 2010, 6, e1001084.
63. S. M. Hersch, H. Yi, C. J. Heilman, R. H. Edwards and A. I. Levey, *The Journal of Comparative Neurology*, 1997, 388, 211-227.
64. K. M. Erikson, C. E. John, S. R. Jones and M. Aschner, *Environ. Toxicol. Pharmacol.*, 2005, 20, 390-394.